The δ_{LT} Puzzle:

Testing χPT in the Generalized Longitudinal-Transverse Spin Polarizability

---

A New Proposal to Jefferson Lab PAC-31

The Hall A Collaboration

and

A. Camsonne (Spokesperson), P. Bosted,
E. Chudakov, J.-P. Chen (Spokesperson), J. Gomez,
J.-O. Hansen, D. Higinbotham, J. Lerose, S. Nanda, A. Saha
Thomas Jefferson National Accelerator Facility, Newport News VA, 23606

D. Crabb, D. Day, R. Lindgren,
N. Liyanage, B. Norum, O.A. Rondon, J. Singh,
K. Slifer[†] (Spokesperson), C. Smith, S. Tajima, K. Wang
University of Virginia, Charlottesville, VA, Charlottesville, VA 22903

N. Kochelev
Bogoliubov Laboratory of Theoretical Physics, JINR, Dubna, Moscow, 141980 Russia
also *Seoul National University,Seoul 151-747, Korea*

X. Li, S. Zhou
China Institute of Atomic Energy, Beijing China

T. Averett, R. J. Feuerbach, V. Sulkosky
The College of William and Mary, Williamsburg, VA 23187

P. Markowitz
Florida International University, Miami, Fl 33199

E. Cisbani, F. Cusanno, S. Frullani, F. Garibaldi
INFN Roma1 gr. coll. Sanita', Rome, Italy

G.M. Urciuoli
INFN Roma1, Rome, Italy

R. De Leo, L. Lagamba, S. Marrone
INFN Bari, Bari, Italy

M. Iodice
INFN Roma3, Rome, Italy

S. Širca
Dept. of Physics, University of Ljubljana, Slovenia

W. Bertozzi, S. Gilad,
J. Huang, B. Moffit, P. Monaghan,
N. Muangma, A. Pucket, Y. Qiang, X.-H. Zhan
Massachusetts Institute of Technology, Cambridge, MA 02139

F. R. Wesselmann
Norfolk State University, Norfolk, VA 23504

K. McCormick
Pacific Northwest National Laboratory, Richland, WA 99352

R. Gilman[⋆], G. Kumbartzki
Rutgers, The State University of New Jersey, Piscataway, NJ 08854
[⋆]also *Thomas Jefferson National Accelerator Facility, Newport News VA, 23606*

Seonho Choi, Ho-young Kang, Hyekoo Kang,
Byungwuek Lee, Yoomin Oh, Jeongseog Song
Seoul National University, Seoul 151-747, Korea

B. Sawatzky
Temple University, Philadelphia PA, 19122

H. Lu, X. Yan, Y. Ye, Y. Jiang
University of Sci. and Tech. of China , Hefei, Anhui, China

†Contact person: Karl Slifer, slifer@jlab.org

Abstract

Recent experimental data on nucleon spin structure at low to intermediate momentum transfers has provided valuable new information in the confinement regime, and shed light on the transition from confinement to asymptotic freedom. New insight has been gained by exploring moments of the spin structure functions and their corresponding sum rules. At low Q^2, Chiral Perturbation Theory (χPT) has emerged as the effective theory of QCD. χPT calculations agree reasonably well with the first moment of the spin structure function g_1^p up to $Q^2 \approx 0.06$ GeV^2, and the generalized forward spin polarizability γ_0^n at $Q^2 = 0.1$ GeV^2. However, χPT calculations have failed to reproduce the neutron data in the case of the generalized L-T spin polarizability δ_{LT}^n. This 'δ_{LT} puzzle' has presented a significant challenge to our understanding of the dynamics of QCD in the chiral perturbation region. It is of great importance to test the isospin dependence and determine if this discrepancy exists for the proton also.

To form the polarizability δ_{LT}^p, a measurement of g_2^p is needed. Due to the technical challenges that arise from a transversely polarized proton target, only g_1^p data have been taken at low momentum transfer. We request 24 days in order to perform a measurement of $\delta_{LT}^p(Q^2)$ with 8% systematic uncertainty in the Q^2 range where χPT is expected to work well. The statistical accuracy will be comparable to the systematic and will allow an unambiguous test of the χPT calculations.

Contents

1 Theoretical Background and Motivation

1.1 Introduction

In the last twenty-five years, the experimental and theoretical study of the spin structure of the nucleon has provided many exciting results, along with new challenges [1]. This investigation has involved testing QCD in its perturbative regime via spin sum rules like the Bjorken sum rule [2], and understanding how the spin of the composite nucleon arises from the intrinsic degrees of freedom of the theory.

Recently, results have become available from a new generation of JLab experiments that seek to probe the theory in its non-perturbative and transition regimes. Distinct features seen in the nucleon response to the electromagnetic probe indicate that complementary descriptions of the interaction are possible, depending on the resolution of the probe. The low momentum-transfer results offer insight into the coherent region where the collective behavior of the nucleon constituents give rise to the static properties of the nucleon, in contrast to the scaling regime, where quark-gluon correlations are suppressed.

Theoretically, the low energy (or low Q^2) region can be described by a QCD-based effective theory : Chiral Perturbation Theory (χPT). Recently, χPT has been used as a powerful tool to help Lattice QCD (LQCD) to extrapolate to the physical region. One example is the use of the Chiral extrapolation in π mass from a few hundred MeV to the physical mass scale, and from finite to infinite volume. In view of this interplay between χPT and LQCD, it is critical to have benchmark tests of the reliability of χPT calculations.

The JLab experiments [3]– [12] on the spin structure of the nucleon have extracted the spin structure functions g_1^n, g_2^n and g_1^p and their moments over a wide kinematic range. These moments have proven to be powerful tools to test QCD sum rules and Chiral Perturbation Theory calculations. However, at the low Q^2 relevant to χPT, data on the g_2^p structure function is conspicuously absent. Currently, the lowest momentum transfer that has been investigated [8] is $Q^2 \approx 1.3$ GeV^2. The absence of transverse data is particularly unsatisfying given the intriguing results found in the transverse neutron data: The SLAC E155 collaboration [13] found a three sigma violation of the proton Burkhardt-Cottingham sum rule at $Q^2 = 5.0$ GeV^2, while the E94010 collaboration [3] found that the neutron BC sum rule held within the experimental uncertainty below $Q^2 = 1.0$ GeV^2 (see Fig. 3). Even more compelling, it was found that state-of-the-art NLO[‡] χPT calculations are in agreement with the neutron data for the generalized polarizability γ_0^n at $Q^2 = 0.1$ GeV^2, but exhibit a significant discrepancy with the longitudinal-transverse polarizability δ_{LT}^n (see Fig. 1). This is particularly surprising since δ_{LT} is insensitive to the Δ resonance contribution which is not well under control in the χPT calculations. For this reason, it was believed that δ_{LT} should be more suitable than γ_0 to serve as a testing ground for the chiral dynamics of QCD [14, 15]. It is natural to ask if this discrepancy exists in the proton case, and determining the isospin dependence will help to solve the δ_{LT} puzzle.

[‡]Next to leading order

From discussions with theorists, this discrepancy might originate from the short range part of the interaction. Some possible mechanisms which might be responsible are t-channel axial vector meson exchange [17, 18], or an effect of QCD vacuum structure [19]. It is essential to separate different isospins in the t-channel in order to understand the mechanism.

1.2 Sum Rules and Moments

Sum rules involving the spin structure of the nucleon offer an important opportunity to study QCD. In recent years the Bjorken sum rule at large Q^2, and the Gerasimov-Drell-Hearn (GDH) sum rule [20] at $Q^2 = 0$, have attracted a concerted experimental and theoretical effort (see for example [21]) that has provided us with rich information. Another class of sum rules address the generalized GDH sum [22] and the spin polarizabilities [23]. These sum rules which are based on "unsubtracted" dispersion relations and the optical theorem relate the moments of the spin structure functions to real or virtual Compton amplitudes, which can be calculated theoretically.

Considering the forward spin-flip doubly-virtual Compton scattering (VVCS) amplitude g_{TT}, and assuming it has an appropriate convergence behavior at high energy, an unsubtracted dispersion relation leads to the following equation for g_{TT} [9, 23]:

$$\mathrm{Re}[g_{TT}(\nu, Q^2) - g_{TT}^{pole}(\nu, Q^2)] = (\frac{\nu}{2\pi^2})\mathcal{P}\int_{\nu_0}^{\infty} \frac{K(\nu', Q^2)\sigma_{TT}(\nu', Q^2)}{\nu'^2 - \nu^2} d\nu', \quad (1)$$

where g_{TT}^{pole} is the nucleon pole (elastic) contribution, $\mathcal{P}$ denotes the principal value integral and K is the virtual photon flux factor. The lower limit of the integration ν_0 is the pion-production threshold on the nucleon. A low-energy expansion gives:

$$\mathrm{Re}[g_{TT}(\nu, Q^2) - g_{TT}^{pole}(\nu, Q^2)] = (\frac{2\alpha}{M^2})I_{TT}(Q^2)\nu + \gamma_0(Q^2)\nu^3 + O(\nu^5). \quad (2)$$

Combining Eqs. (1) and (2), the $O(\nu)$ term yields a sum rule for the generalized GDH integral [21, 22]:

$$\begin{aligned} I_{TT}(Q^2) &= \frac{M^2}{4\pi^2\alpha}\int_{\nu_0}^{\infty} \frac{K(\nu, Q^2)}{\nu}\frac{\sigma_{TT}}{\nu} d\nu \\ &= \frac{2M^2}{Q^2}\int_0^{x_0} \Big[g_1(x, Q^2) - \frac{4M^2}{Q^2}x^2 g_2(x, Q^2)\Big] dx. \end{aligned} \quad (3)$$

The low-energy theorem relates I(0) to the anomalous magnetic moment of the nucleon, κ, and Eq. (3) becomes the original GDH sum rule [20]:

$$I(0) = \int_{\nu_0}^{\infty} \frac{\sigma_{1/2}(\nu) - \sigma_{3/2}(\nu)}{\nu} d\nu = -\frac{2\pi^2\alpha\kappa^2}{M^2}, \quad (4)$$

where $2\sigma_{TT} \equiv \sigma_{1/2} - \sigma_{3/2}$. The $O(\nu^3)$ term yields a sum rule for the generalized forward spin polarizability [23]:

$$\begin{aligned}\gamma_0(Q^2) &= (\frac{1}{2\pi^2})\int_{\nu_0}^{\infty}\frac{K(\nu,Q^2)}{\nu}\frac{\sigma_{TT}(\nu,Q^2)}{\nu^3}d\nu \\ &= \frac{16\alpha M^2}{Q^6}\int_0^{x_0} x^2\Big[g_1(x,Q^2) - \frac{4M^2}{Q^2}x^2 g_2(x,Q^2)\Big]dx. \end{aligned} \quad (5)$$

Considering the longitudinal-transverse interference amplitude g_{LT}, the $O(\nu^2)$ term leads to the generalized longitudinal-transverse polarizability [23]:

$$\begin{aligned}\delta_{LT}(Q^2) &= (\frac{1}{2\pi^2})\int_{\nu_0}^{\infty}\frac{K(\nu,Q^2)}{\nu}\frac{\sigma_{LT}(\nu,Q^2)}{Q\nu^2}d\nu \\ &= \frac{16\alpha M^2}{Q^6}\int_0^{x_0} x^2\Big[g_1(x,Q^2) + g_2(x,Q^2)\Big]dx. \end{aligned} \quad (6)$$

Alternatively, we can consider the covariant spin-dependent VVCS amplitudes S_1 and S_2, which are related to the spin-flip amplitudes g_{TT} and g_{LT}. The unsubtracted dispersion relations for S_2 and νS_2 lead to a "super-convergence relation" that is valid for any value of Q^2,

$$\int_0^1 g_2(x,Q^2)dx = 0, \quad (7)$$

which is the Burkhardt-Cottingham (BC) sum rule [24].

1.3 Recent Results from Jefferson Lab

1.3.1 Spin Polarizabilities: γ_0 and δ_{LT} for the Neutron

The generalized spin polarizabilities provide benchmark tests of χPT calculations at low Q^2. Since the generalized polarizabilities have an extra $1/\nu^2$ weighting compared to the first moments, these integrals have only a small contribution from the large-ν region and converge much faster, which minimizes the uncertainty due to extrapolation. Measurements of the generalized spin polarizabilities are an important step in understanding the dynamics of QCD in the chiral perturbation region. At low Q^2, the generalized polarizabilities have been evaluated with next-to-leading order χPT calculations [14, 15]. One issue in the χPT calculations is how to properly include the nucleon resonance contributions, especially the Δ resonance. As was pointed out in Refs. [14, 15], while γ_0 is sensitive to resonances, δ_{LT} is insensitive to the Δ resonance.

The first results for the neutron generalized forward spin polarizabilities $\gamma_0(Q^2)$ and $\delta_{LT}(Q^2)$ were obtained at Jefferson Lab Hall A [3]. The results for $\gamma_0^n(Q^2)$ are shown in the top panel of Fig. 1. The statistical uncertainties are smaller than the size of the symbols. The data are compared with a next-to-leading order ($O(p^4)$) HBχPT[§]

[§]Heavy Baryon Chiral Perturbation Theory

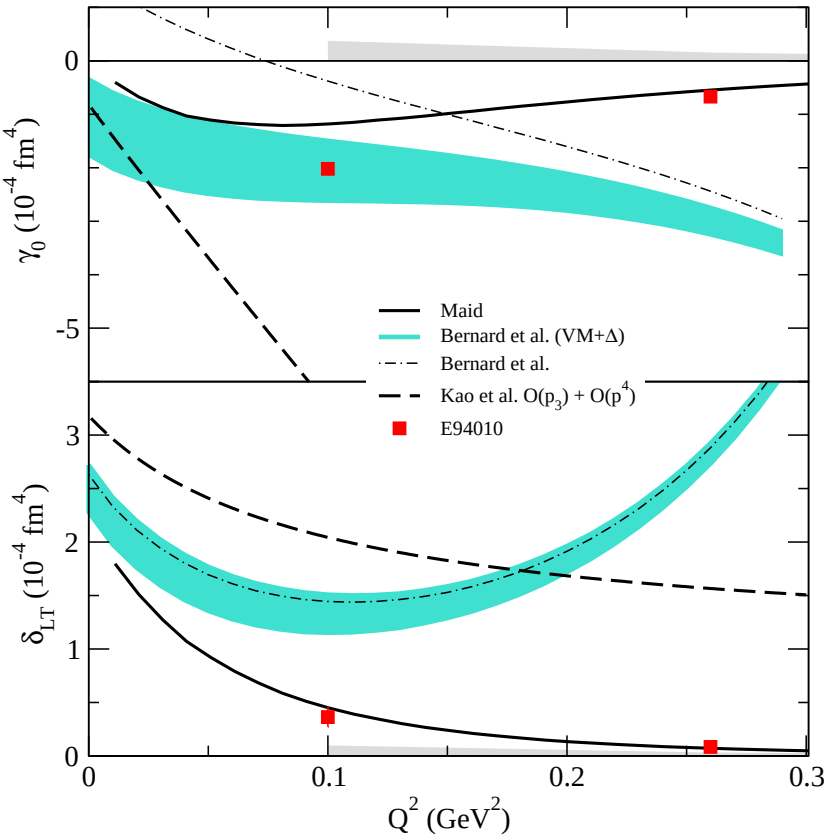

Figure 1: The neutron spin polarizabilities γ_0 (top) and δ_{LT} (bottom). Solid squares represent the results from [3] with statistical uncertainties. The light grey band on the axis represents systematic uncertainties. The heavy dashed curve is the HBχPT calculation of Kao *et al.* [15]. The dot-dashed curve (blue band) is the RBχPT calculation of Bernard *et al.* [14] without (with) the Δ and vector meson contributions. The solid curve is the MAID model [21].

calculation [15], a next-to-leading order RBχPT[¶] calculation [14], and the same calculation explicitly including both the Δ resonance and vector meson contributions. Predictions from the MAID model [21] are also shown. At the lowest Q^2 point, the RBχPT calculation including the resonance contributions is in good agreement with the experimental result. For the HBχPT calculation without explicit resonance contributions, discrepancies are large even at $Q^2 = 0.1$ GeV^2. This might indicate the significance of the resonance contributions or a problem with the heavy baryon approximation at this Q^2. The MAID model reproduces the higher Q^2 data point but underestimates the strength at $Q^2 = 0.1$ GeV^2.

Since δ_{LT} is insensitive to the Δ resonance contribution, it was believed that δ_{LT} should be more suitable than γ_0 to serve as a testing ground for the chiral dynamics of QCD [14, 15]. Fig. 1 shows δ_{LT} compared to χPT calculations and the MAID predictions. While the MAID predictions are in good agreement with the results, it is surprising to see that the data are in significant disagreement with the χPT calculations even at the lowest Q^2, 0.1 GeV^2. This disagreement presents a significant challenge to the present implementation of Chiral Perturbation Theory.

1.3.2 $d_2(x, Q^2)$

The $d_2(Q^2)$ matrix element provides an efficient way to study the high Q^2 behavior of the nucleon spin structure. At large Q^2, it is related to the color polarizabilities and can be calculated from Lattice QCD. At lower Q^2, it provides a means to study the transition from perturbative to non-perturbative behaviour, and to quantify higher twist effects. In DIS, the leading twist contribution to g_2 is given by the Wandzura-Wilczek [25] relation:

$$g_2^{WW}(x, Q^2) = -g_1(x, Q^2) + \int_0^1 g_1(y, Q^2)\frac{dy}{y} \tag{8}$$

d_2 quantifies the higher twist contribution to g_2 via:

$$d_2 = 3\int_0^1 x^2 \left(g_2 - g_2^{WW}\right) dx \tag{9}$$

$$= \int_0^1 x^2 \left[2g_1 + 3g_2\right] dx \tag{10}$$

In practice, we do not access the entire kinematic region ($0 < x < 1$). To signify this, and the fact that we are at finite Q^2, the symbol $\bar{d}_2$ is often used. In Fig. 2, recent neutron $\bar{d}_2(Q^2)$ data is shown. The experimental results are the open circles, while the grey band represents the systematic uncertainty. The world neutron results from SLAC [13] (open square) and from JLab E99-117 [34] (solid square) are also shown. The solid line is the MAID calculation [21] which includes only the resonance contribution.

[¶]Relativistic Baryon Chiral Perturbation Theory

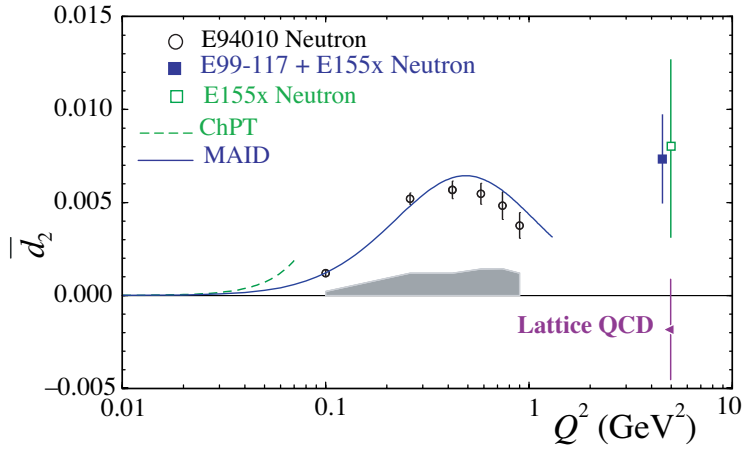

Figure 2: $\bar{d}_2^n$ results from JLab [3, 34] and SLAC [13], together with the Lattice QCD calculations [33], and the MAID [21] model.

At low Q^2, the HBχPT calculation of Kao *et al.* [15] is shown with a dashed line. The RBχPT of Bernard *et al.* [14] is very close to the HBχPT curve at this scale, regardless of whether the authors include vector mesons and the Δ contributions. It is not shown on the figure for clarity. The Lattice QCD prediction [33] at Q^2 = 5 GeV^2 is negative but close to zero, and represents a 2σ deviation from the experimental result. We note that all available models (not shown) predict a negative or zero value at large Q^2. As Q^2 increases, the data reveal a positive, but decreasing $\bar{d}_2^n$.

Other preliminary results for the neutron [12] at a Q^2 range of 1-4 GeV^2, and for the proton and deuteron [8] at $Q^2 \approx 1.3$ GeV^2 are available now.

1.3.3 The Burkhardt-Cottingham Sum Rule

Fig. 3 shows the Burkhardt-Cottingham integral (see Eq. 7) for the neutron, which was extracted from Hall A experiment E94-010 [3], from pion threshold to $W = 2$ GeV. The capability to transversely polarize the Hall A ^{3}He target allowed for the precise measurements of g_2 needed for the BC sum. The measured region is shown with solid circles, and the MAID estimate should be compared directly to these resonance region points. The open diamonds represent the full ($0 < x < 1$) integral, which is evaluated using the well know elastic form factors for the $x = 1$ contribution, and assuming $g_2 = g_2^{WW}$ in the unmeasured low-x region. The upper, lower bands correspond to the experimental systematic errors, and the estimate of the systematic error for the low-x extrapolation, respectively. The total integral exhibits a striking cancellation of the in-

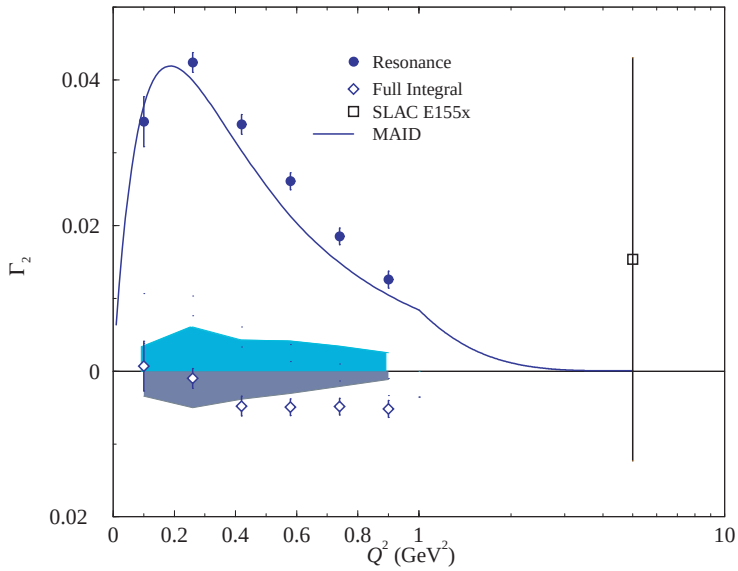

Figure 3: Neutron $\Gamma_2(Q^2)$. Full circle : resonance contribution, compared with the MAID model [21]. Open diamonds are the full ($0 < x < 1$) integral, including estimates for the elastic and low-x contributions. Upper, lower bands correspond to the experimental systematic errors, and the systematic error of the low-x extrapolation, respectively. SLAC E155x [13] data at $Q^2 = 5$ GeV^2 is also shown.

elastic (resonance+DIS) and elastic contributions, leading to an apparent satisfaction of the Burkhardt-Cottingham sum rule within uncertainties. The SLAC E155x collaboration [13] previously reported a neutron result at high Q^2 (open square), which is consistent with zero but with a rather large error bar. On the other hand, the SLAC proton result deviated from the BC sum rule prediction by 3 standard deviations [13].

1.3.4 The First Moment of g_1

Fig. 4 displays the preliminary proton results for $\bar{\Gamma}_1(Q^2)$ from the EG1b [7] experiment, together with the published results from EG1a [4, 5], SLAC [13] and HERMES [26]. The error bar indicates the statistical uncertainty while the band on the axis represents the systematic uncertainty.

At $Q^2 = 0$, the slope of Γ_1 is predicted by the GDH sum rule. χPT calculations by Ji *et al.* [27] using HBχPT, and by Bernard *et al.* [14] with and without the inclusion of vector mesons and Δ degrees of freedom are also shown. The χPT calculations start to show disagreement with the data above $Q^2 \approx 0.06$ GeV^2. At moderate and large Q^2, the data are compared with two model calculations [28, 29], both of which reproduce the data reasonably well.

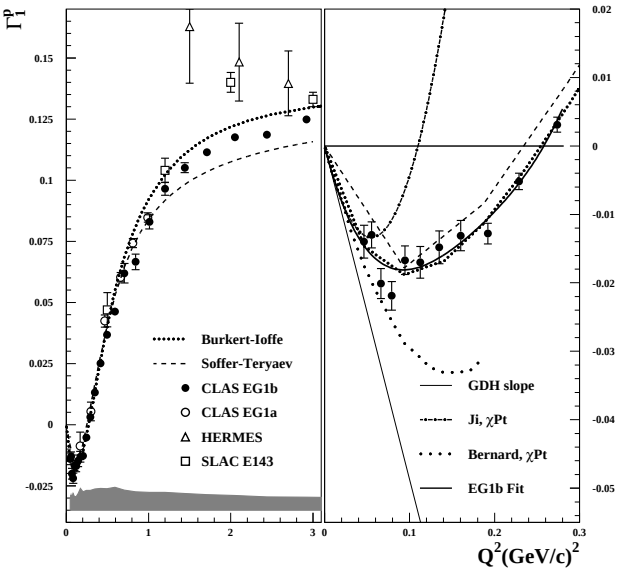

Figure 4: Preliminary proton $\Gamma_1(Q^2)$ from EG1b [7], together with published results from EG1a [4], SLAC [13] and HERMES [26]. Model predictions from the Soffer-Teryaev [28] and Burkert-Ioffe [29]. The insets show comparisons with the NLO χPT predictions by Ji *et al.* [27], and Bernard *et al.* [14].

1.3.5 Ongoing Analyses

Several recent spin structure experiments are in the process of analyzing existing data. These results should be available soon. For example, an extraction of γ_0^p will be performed from the EG1b $A_{\|}$ data [30] down to $Q^2 \approx 0.05$ GeV^2. The preliminary results [30] show a large deviation from the χPT calculations of Refs. [14, 15]. Neutron(^{3}He) longitudinal and transverse data [10] has also been taken at Q^2 down to 0.02 GeV^2. A longitudinal measurement aimed at extracting g_1 for the proton and deuteron [11] reached similar Q^2. Preliminary results [8, 35] for the proton d_2 and BC integral at $Q^2 = 1.3$, will also soon be available.

1.3.6 Experimental Status Summary

In summary, a large body of nucleon spin-dependent cross-section and asymmetry data have been collected at low to moderate Q^2 in the resonance region. These data have been used to evaluate the Q^2 evolution of moments of the nucleon spin structure functions g_1 and g_2, including the GDH integral, the Bjorken sum, the BC sum and the spin polarizabilities. The BC sum rule for the neutron is observed to be satisfied within uncertainties due to a cancellation between the inelastic and elastic contributions. The situation for the proton is less clear, with a three sigma violation found at $Q^2 = 5$ GeV^2.

At low Q^2, available next-to-leading order χPT calculations have been tested against data and found to be in reasonable agreement for $0.05 < Q^2 < 0.1$ GeV^2 for the GDH integral $I(Q^2)$, $\Gamma_1(Q^2)$ and the forward spin polarizability $\gamma_0(Q^2)$. Although it was expected that the χPT calculation of δ_{LT} would offer a faster convergence because of the absence of the Δ contribution, the experimental data show otherwise. None of the available calculations can reproduce δ_{LT} at Q^2 of 0.1 GeV^2. This discrepancy presents a significant challenge to our theoretical understanding of χPT.

To better understand the δ_{LT} puzzle, or more importantly, to better understand what the puzzle means in terms of the Chiral dynamics, we need both theoretical and experimental efforts. A natural question is whether this discrepancy also exists in the proton case. Testing the isospin dependence would help shed light on the problem. However, there has been no measurement with a transversely polarized proton target for $Q^2 < 1.3$ GeV^2, and there is consequently no experimental data for δ_{LT}^p. It is of great interest to have a measurement of δ_{LT}^p in the low Q^2 region where the Chiral Perturbation Theory calculations are expected to work.

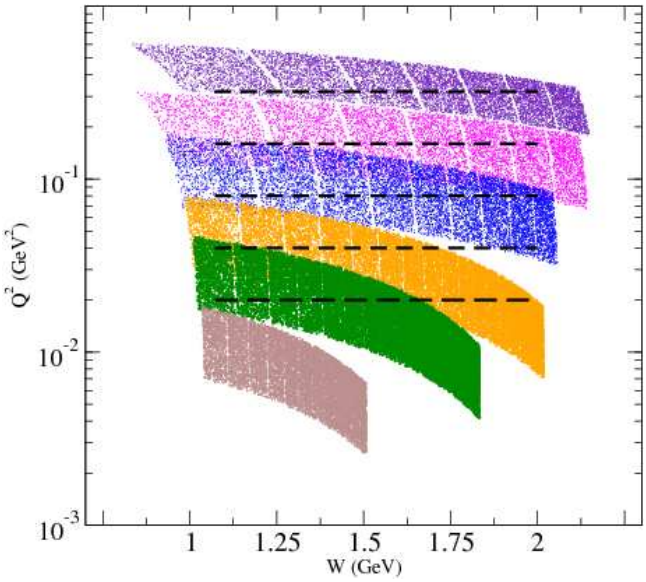

Figure 5: Kinematic coverage. Specific beam and angle values are detailed in Table 4. Dashed lines represent the the constant Q^2 values where δ_{LT} and the BC Sum will be evaluated.

2 Proposed Experiment

We plan to perform an inclusive measurement at forward angle of the proton spin-dependent cross sections in order to determine the g_2^p structure function in the resonance region for $0.02 < Q^2 < 0.4$ GeV^2. This measurement will allow an extraction of the generalized longitudinal-transverse spin polarizability δ_{LT}, and a test of the Burkhardt-Cottingham sum rule.

The kinematic coverage, shown in Fig. 5, complements experiement EG4 [11]. Data will be measured in the transverse configuration for all energies. In addition, beamtime will be dedicated to the longitudinal configuration for one energy, in order to provide some overlap and cross check of the EG4 data. Kinematic details are listed in Table 4.

This experiment will require the baseline Hall A equipment, with the addition of the septa magnets, and the JLab/UVa polarized target. Adapting the polarized target to Hall A will require extensive technical support from JLab. In particular, we will request:

1. Installation of the UVA/JLab 5 T polarized target.

2. Installation of an upstream chicane and associated support structures.

3. Temporary removal of the eP detector in order to place the chicane magnets.
4. Installation of the slow raster, and the Basel Secondary Emission Monitor (SEM).
5. Installation of a local beam dump.
6. Operation of the beamline instrumentation for 50-100 nA beam.

We examine these requirements in detail in the following sections.

2.1 Polarized Target

The polarized target (has been successfully used in experiments E143/E155/E155x at SLAC and E93-026 and E01-006 at JLab. This target operates on the principle of Dynamic Nuclear Polarization, to enhance the low temperature (1 K), high magnetic field (5 T) polarization of solid materials (ammonia, lithium hydrides) by microwave pumping. The polarized target assembly contains several target cells of variable length (0.5-3.0 cm) that can be selected individually by remote control to be located in the uniform field region of a superconducting Helmholtz pair. The permeable target cells are immersed in a vessel filled with liquid Helium and maintained at 1 K by use of a high power evaporation refrigerator.

The target material is exposed to 140 GHz microwaves to drive the hyperfine transition which aligns the nucleon spins. The DNP technique produces proton polarizations of up to 90% in the NH_3 target. The heating of the target by the beam causes a drop of a few percent in the polarization, and the polarization slowly decreases with time due to radiation damage. Most of the radiation damage is repaired by annealing the target at about 80 K, until the accumulated dose reached is greater than about 17×10^{15} e^-/cm^2, at which time the target material needs to be replaced. The luminosity of the polarized material in the uniform field region is approximately 85×10^{33} cm^{-2} Hz.

2.2 Chicane

To access g_2^p, the polarization direction will be held perpedicular to the beam axis for the majority of the experiment. This will create a non-negligible deflection of low energy electrons, so to ensure proper transport of the beam, the existing Hall C BE and BZ1 upstream chicane magnets (as used in E93-026 [51]) will be required. In order to fit the dipole magnets into the limited space of the Hall A beamline, we will request the temporary removal of the eP detector for this experiment.

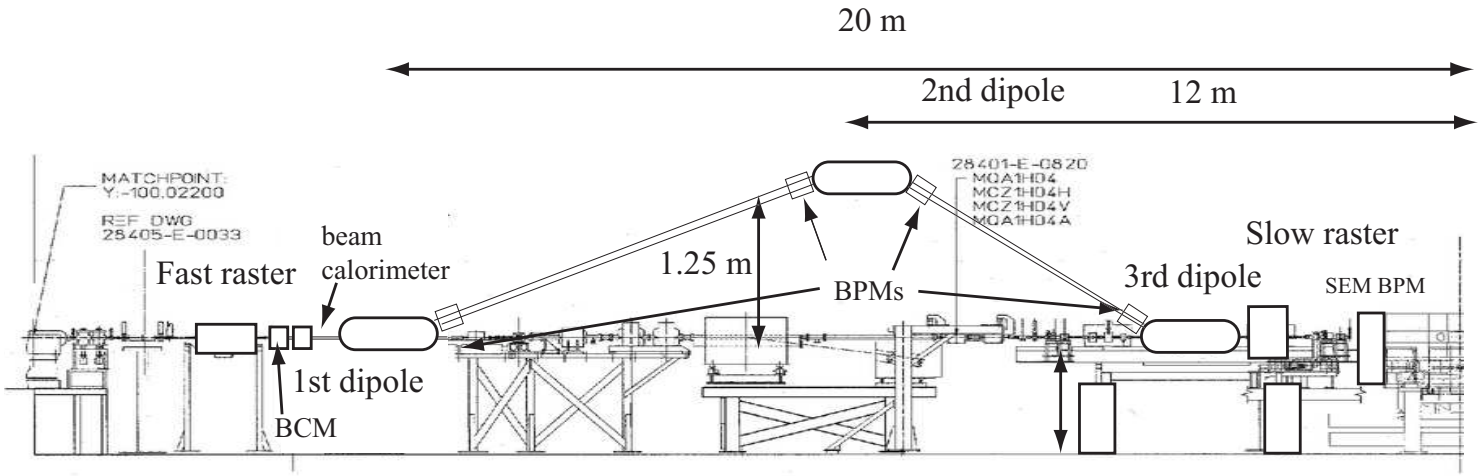

Figure 6: Beamline schematic indicating the location of the fast/slow rasters, Secondary Emission Monitor (SEM), tungsten calorimeter and the chicane magnets. The third dipole will be located on a hydraulic stand in order to accomodate the range of vertical displacements (see Table 1) required. Distances are with respect to the polarized target center, at the far right of the diagram.

Energy (GeV)	Deflection Angle (deg)
1.1	11.7
1.7	7.6
2.2	5.9
3.3	3.9
4.4	2.9

Table 1: Vertical deflection of the incident electron beam due to the 5 T target field.

The chicane placement is detailed in Fig. 6. Two dipoles will be located at 20 and 12 m upstream of the target, respectively. Table 1 lists the deflection angles that will be created by the 5 T target field for each incident energy. A third dipole similar to the one used for the Compton polarimeter chicane will be used to accomodate the relatively small deflection angle at the highest energies. The range of needed vertical displacements will be accomodated by placing this last dipole on a hydraulic stand as was done in hall C. Beam Position Monitors (BPMs) will be placed along the chicane line before and after each magnet to ensure proper transport of the beam.

2.3 Raster

The existing Hall A fast raster will be used to generate a pattern up to 4 mm x 4 mm and will remain in its standard location (see Fig. 6). The slow raster will be located just upstream of the target, and can increase the final size up to 2.5 cm x 2.5 cm, although we will use a smaller spotsize. A 2 inch wide beam pipe will be used starting after the slow raster.

2.4 Secondary Emission Monitor

To ensure proper reconstruction of target variables given the large raster size, we will utilize the Basel Secondary Emission Monitor (SEM)[‖]. This device was used under similar conditions in Hall C and provided an accuracy of better than 1 mm for currents as low as 10 nA. It is insensitive to the target magnetic field.

2.5 Exit beam pipe and beam dump

The low currents employed in this experiment allow for the use of a local beam dump[**], just downstream of the target. The connection from the vacuum chamber to the exit beam pipe will need to be modified to accommodate the vertical deflection of the beam,

[‖] Also referred to as SEE for **s**econdary **e**lectron **e**mission.

[**] as was done for the Hall C RSS and GEn experiments

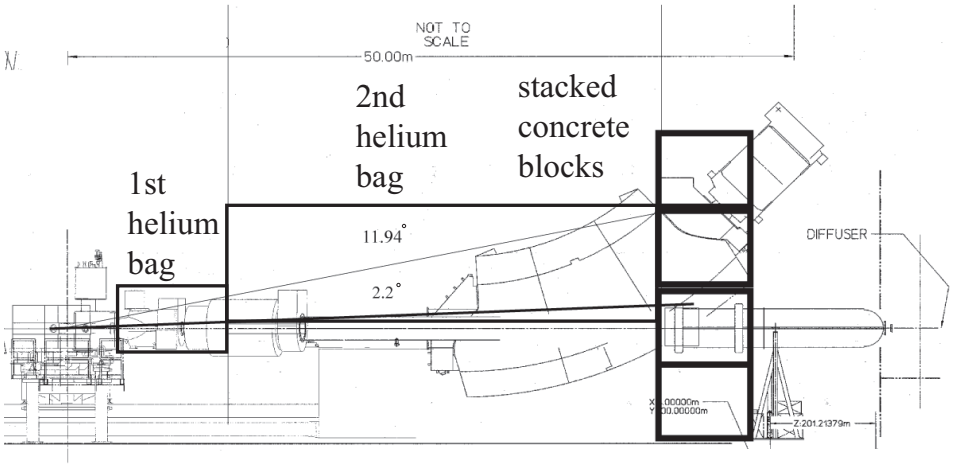

Figure 7: Schematic of beam exit and local dump.

and the coupling to the beam pipe going to the beam dump. We plan to move the target position upstream by 25 cm, in order to produce a two inch gap between the two septa at six degrees. A two inch beam pipe is sufficient to accomodate the rastered beam and expected multiple scattering.

A helium bag will be used to transport the beam past the septa. This allows for different exit angles. Connection to the usual beam pipe will be made at 5 meters downstream, in order to allow for 'straight-thru' passage of the beam to the standard beam dump when necessary: for example during Moller measurements and beam tuning. A 10 inch diameter beam pipe will accomadate all planned scenarios. The beam dump (see Fig. 7) will be constructed above the beam line by stacking concrete blocks movable with the crane.

2.6 Beamline Instrumentation

2.6.1 Beam Current and Beam Charge Monitor

Beam currents less than 100 nA are typically used with the polarized target in order to limit depolarizing effects and large variations in the density. Standard BCM cavities have a linearity good to 0.2% for currents ranging from 180 down to 1 uA. High accuracy at even lower currents will be possible due to ongoing upgrades, which will be complete before this proposal might be scheduled. Most notably, the Happex III [50] and Lead Parity experiments will require accurate knowledge of the charge and beam position down 50 nA. We plan to use the low current cavity monitor BCM/BPM sets

that were initially tested in 2005. In addition, experiment E05-004[48] has just recently commissioned a tungsten beam calorimeter, in order to have a good calibration for $I < 3\mu A$. Preliminary results show an absolute calibration of the Hall A BCM with 1% accuracy for currents ranging from 3 μA down to 0.5μA. The calorimeter will be located just after the first BPM and before the first dipole (see Fig. 6). In the worst-case scenario, the tungsten calorimeter will allow at least 2% accuracy [49] on the charge determination all the way down to 50 nA.

2.6.2 Beam Polarimetry

We will utilize the Moeller polarimeter as part of the standard Hall A equipment. During operation, 0.3 to 0.5 μA of current are incident on a foil of iron polarized by a magnetic field. The expected systematic uncertainty [52] of the Moeller measurement is 3.5% or better. An upgrade is planned for the Lead Parity experiment with the goal of reaching 1% systematic. Moeller runs will be scheduled at least once per energy change, and will will be performed with the (non-chicaned) beam passing to the standard hall A dump.

The Compton polarimeter normally is used for a continuous non-invasive beam polarization monitor. However, it is not very well suited to run at low energy or low current. To provide a cross check of the Moller polarimeter, we may dedicate some high current beam time (without polarized target) specifically for Compton polarimeter measurements.

2.7 The Spectrometers

2.7.1 Septa Magnet

The Hall A spectrometers will be fitted with septa magnets allowing to reach scattering angles of 6 and 9 degrees. They have been used successfully for the Hypernuclear experiment, Happex and small angle GDH, so their optical properties are well understood.

2.7.2 Detector Stack

The standard detector stack will be used for detecting electrons. We will require the usual VDC, scintillators S1 and S2, the gas Cerenkov and pion rejector/shower counter for particle identification. Performance of the spectrometers are well known so we can expect the same accuracies as for the GDH experiment on the polarized He3 target E94-010 and E97-110. We note that pion contamination at these kinematics is negligible, as indicated from the epc [53] simulation code.

2.7.3 Optics

A study of the change of the optics coming from the target field was done by John Lerose for the lowest anticipated electron momentum (400 MeV/c). Fig. 8 shows the

scattered electrons without field. Fig. 9 displays the effect of the 5 Tesla field. Fig. 10 shows the incident beam corrected by the chicane so that it is horizontal at the target. Except for an approximate 5 mm vertical offset, (which would give about 10^{-3} offset in detected momentum), the shifted envelope looks very much like the no-field situation when it gets to the entrance of the septum. The effect would diminish linearly with either an increase in momentum, or a decrease in the magnetic field. The situation, from an optics point of view, appears to be manageable even in this worst case scenario.

For further detail, Figs. 11 to 14 demonstrate the effect of the 5 T target field on the reconstruction [41]. These plots represent a montecarlo simulation of the target variables δ, θ, ϕ, and y_t. Overall, as the scattered electron momentum decreases, there is a slight degradation in resolution. Shifts in θ (vertical) are also seen along with much smaller shifts in δ and ϕ. The offsets do not have a significant effect since the variables remain in the well known region of the acceptance. The degradation of resolution should result in no worse than a factor of two [41] increase in the systematic uncertainty of the acceptance.

2.7.4 Data Acquisition

We will utilize the standard Hall A data acquisition (DAQ) system which is based on Fastbus 1877 TDC and Fastbus 1881 ADC. The DAQ will be run in two single arm mode which allows up to 4 KHz rate of data for each arm. We will be DAQ rate limited for the lowest few energies.

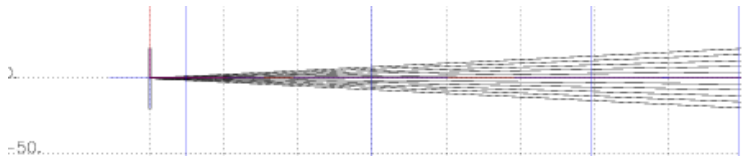

Figure 8: The vertical envelope of 400 MeV/c electron trajectories that would normally go through the spectrometer and septum setup (+-50 mrad).

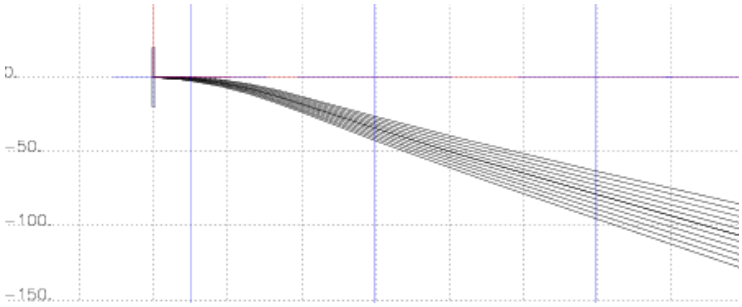

Figure 9: The same envelope of 400 MeV/c trajectories but with the 5 Tesla target field turned on.

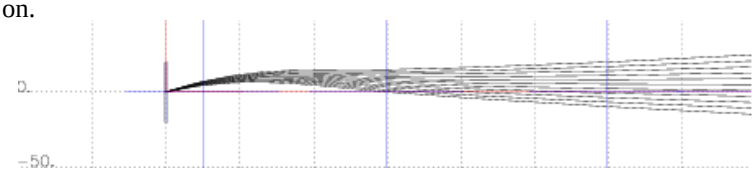

Figure 10: 5 Tesla field remains on but the set of trajectories is vertically shifted by 275 mrad.

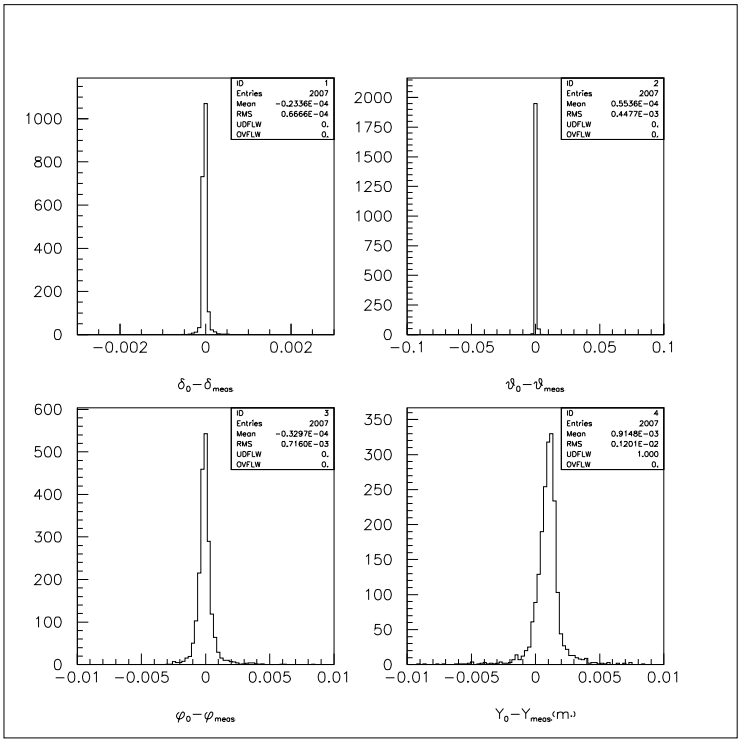

Figure 11: Reconstructed variables : Momentum = 4 GeV/c. Target field = 0 T. **Top left:** momentum spread. **Top right:** vertical scattering angle. **Bottom left:** horizontal scattering angle. **Bottom right:** Y-target.

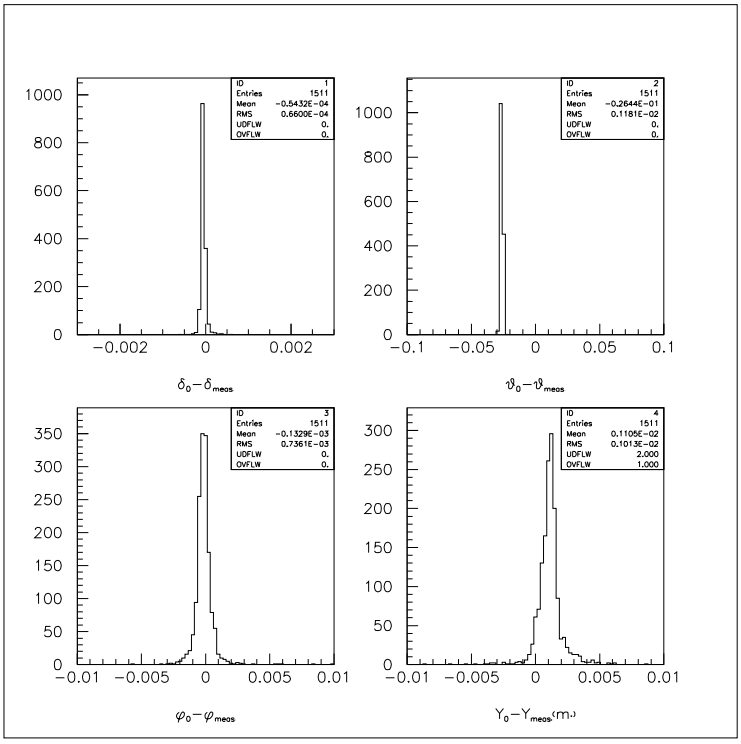

Figure 12: Reconstructed variables : Momentum = 4 GeV/c. Target field = 5 T. **Top left:** momentum spread. **Top right:** vertical scattering angle. **Bottom left:** horizontal scattering angle. **Bottom right:** Y-target.

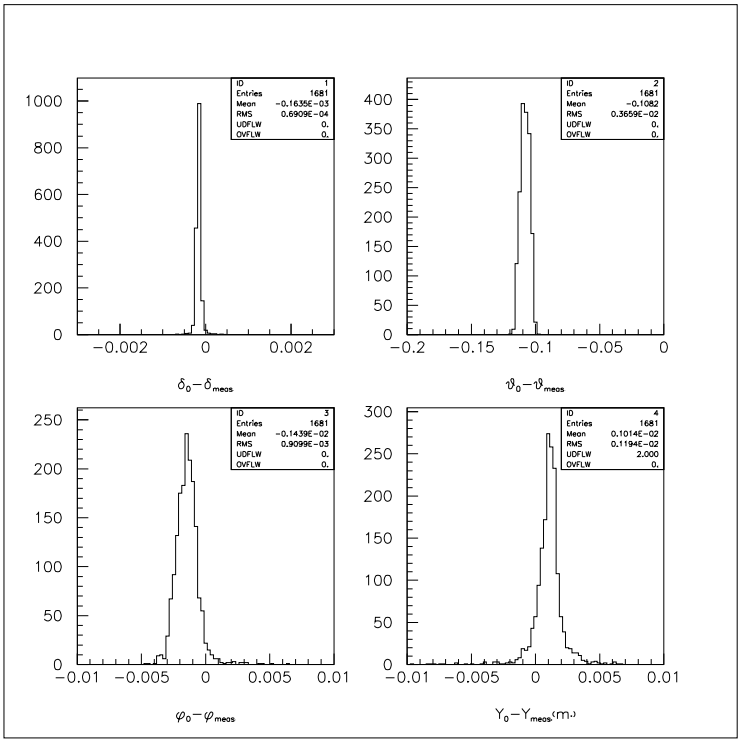

Figure 13: Reconstructed variables : Momentum = 1 GeV/c. Target field = 5 T. **Top left:** momentum spread. **Top right:** vertical scattering angle. **Bottom left:** horizontal scattering angle. **Bottom right:** Y-target.

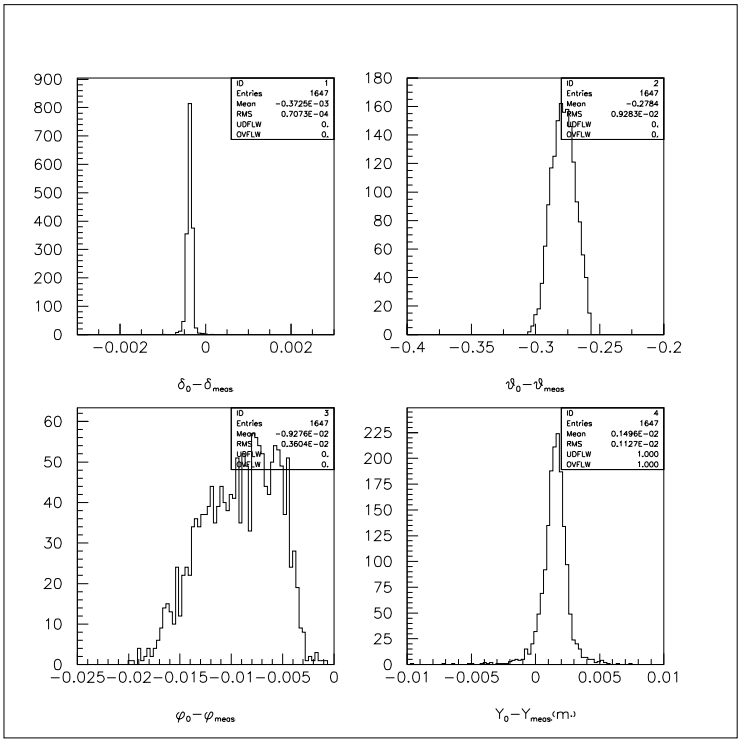

Figure 14: Reconstructed variables : Momentum = 0.4 GeV/c. Target field = 5 T. **Top left:** momentum spread. **Top right:** vertical scattering angle. **Bottom left:** horizontal scattering angle. **Bottom right:** Y-target.

3 Analysis Method

3.1 Extraction of the g_2 Structure Function

We will perform a polarized cross section measurement in order to determine the spin structure function g_2^p. The spin structure functions are related to the spin-dependent cross sections via:

$$\begin{aligned} g_1 &= \frac{MQ^2}{4\alpha_e^2}\frac{y}{(1-y)(2-y)}\left[\Delta\sigma_{\parallel} + \tan\frac{\theta}{2}\Delta\sigma_{\perp}\right] \\ g_2 &= \frac{MQ^2}{4\alpha_e^2}\frac{y^2}{2(1-y)(2-y)}\left[-\Delta\sigma_{\parallel} + \frac{1+(1-y)\cos\theta}{(1-y)\sin\theta}\Delta\sigma_{\perp}\right] \end{aligned} \quad (11)$$

where $y = \nu/E$.

Here, the polarized cross section differences are represented by $\Delta\sigma_{\parallel}$ and $\Delta\sigma_{\perp}$. Measuring polarized cross section differences results in the cancellation of the contribution from any unpolarized target material and obviates the need for any external model input.

We can recast Eq. 11 in the form:

$$\begin{aligned} g_1 &= K_1(a_1\Delta\sigma_{\parallel} + b_1\Delta\sigma_{\perp}) \\ g_2 &= K_2(c_1\Delta\sigma_{\parallel} + d_1\Delta\sigma_{\perp}) \end{aligned} \quad (12)$$

where

$$\begin{aligned} K_1 &= \frac{MQ^2}{4\alpha_e^2}\frac{y}{(1-y)(2-y)} \\ K_2 &= \frac{MQ^2}{4\alpha_e^2}\frac{y^2}{2(1-y)(2-y)} = K_1\frac{y}{2} \\ a_1 &= 1 \\ b_1 &= \tan\frac{\theta}{2} \\ c_1 &= -1 \\ d_1 &= \frac{1+(1-y)\cos\theta}{(1-y)\sin\theta} \end{aligned}$$

Equation 12 reveals that the parallel contribution to g_2 is highly suppressed (See Fig. 15). In fact, the relative weight of the $\Delta\sigma_{\parallel}$ contribution to g_2 ranges from 2 to 8% for all proposed kinematics. For the kinematics where we will not measure $\Delta\sigma_{\parallel}$, we will use the high precision data from Hall B experiment EG4 [11], which expects an uncertainty of approximately 10%. Given the ratio of $|c_1/d_1|$, this leads to less than 1% error contribution to our g_2 for all kinematics.

In practice, the EG4 cross section data is not at the exact same kinematics as our proposal, which makes it difficult to directly combine the respective cross sections.

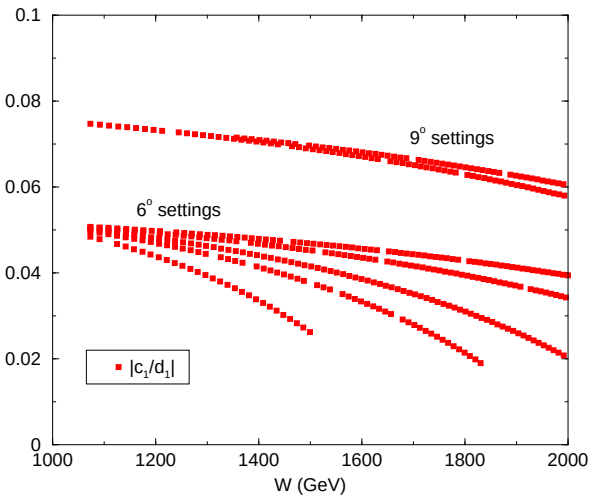

Figure 15: Relative weighting of the $\Delta\sigma_{\parallel}$ contribution to g_2. See Eq. 12.

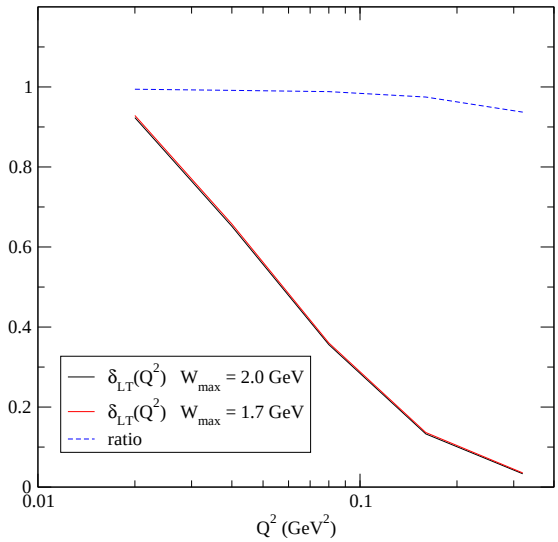

Figure 16: MAID model prediction for $\delta_{LT}(Q^2)$ evaluated with a maximum W of 1.7 and 2.0 GeV, along with the ratio. Over 90% of the integral strength comes from W less than 1.7 GeV.

Instead, we will use the EG4 g_1 data. Inverting Eq. 11 yields:

$$\begin{aligned}
\Delta\sigma_{\parallel} &= \frac{4\alpha_e^2}{MQ^2}\frac{(1-y)(2-y)}{y}\left(\frac{2}{y}\right)\frac{\frac{1+(1-y)\cos\theta}{(1-y)\sin\theta}\frac{y}{2}\,g_1 - \tan\theta/2\,g_2}{\frac{1+(1-y)\cos\theta}{(1-y)\sin\theta}+\tan\theta/2} \\
\Delta\sigma_{\perp} &= \frac{4\alpha_e^2}{MQ^2}\frac{(1-y)(2-y)}{y}\left(\frac{2}{y}\right)\frac{\frac{2}{y}g_1 + g_2}{\frac{1+(1-y)\cos\theta}{(1-y)\sin\theta}+\tan\theta/2}
\end{aligned} \tag{13}$$

Eq. 13 can be recast in the form:

$$\Delta\sigma_{\parallel} = K_3(a_2 g_1 + b_2 g_2) \tag{14}$$
$$\Delta\sigma_{\perp} = K_4(c_2 g_1 + d_2 g_2) \tag{15}$$

where

$$\begin{aligned}
K_3 &= \frac{4\alpha_e^2}{MQ^2}\frac{(1-y)(2-y)}{y}\left(\frac{2}{y}\right)\frac{1}{a_2-b_2} \\
K_4 &= \frac{4\alpha_e^2}{MQ^2}\frac{(1-y)(2-y)}{y}\left(\frac{2}{y}\right)\frac{1}{a_2-b_2} \\
a_2 &= \frac{1+(1-y)\cos\theta}{(1-y)\sin\theta}\frac{y}{2} \\
b_2 &= -\tan\theta/2 \\
c_2 &= \frac{2}{y} \\
d_2 &= 1
\end{aligned}$$

So in terms of the existing Hall B g_1 and the measured $\Delta\sigma_{\perp}$, g_2 can be expressed:

$$g_2 = \left(\frac{1}{1-K_2K_3c_1b_2}\right)\;[d_1\Delta\sigma_{\perp} + K_2K_3c_1a_2\;g_1] \tag{16}$$

3.2 The Generalized Spin Polarizability δ_{LT}

The generalized Longitudinal-Transverse spin polarizability is given in terms of g_1 and g_2 as:

$$\delta_{LT}(Q^2) = \frac{16\alpha M^2}{Q^6}\int_0^{x_0} x^2\Big[g_1(x,Q^2) + g_2(x,Q^2)\Big]dx. \tag{17}$$

For the kinematics where we do not measure g_1 directly we will utilize the results of EG4 [11]. Our proposal includes settings (see Table 4) where we will rotate the target and measure $\Delta\sigma_{\parallel}$ in addition to $\Delta\sigma_{\perp}$ in order to cross check the Hall B data.

Table 7 details the projected EG4 statistical uncertainties [47]. Our beam time request typically aims to match or improve on these errors so that the combined data set is consistent. As for systematic uncertainties, EG4 projects about 10% error, which includes a contribution from their lack of knowledge of transverse data. With our transverse data, their systematic would of course decrease.

3.3 Interpolation to Constant Q^2

The data measured at constant incident energy and scattering angle will be interpolated[†] to constant Q^2 as shown in Fig. 5. The good kinematic coverage and overlap should facilitate a straight forward interpolation.

3.4 Systematic Uncertainties

Several JLab experiments have performed measurements similar to what we propose here (for example, see Refs. [3, 8, 10, 11]). From these previous endeavors, we can make an estimate of the dominant contributions to the systematic uncertainty. Table 2 gives an estimate of the most significant sources of error, while Table 3 gives further detail on the contributions to the cross section uncertainty which will be the dominant error. Previous experience in Hall A [3] has shown that we can obtain 4-5% systematic uncertainy [43, 44, 45] on the cross section, with the dominant uncertainty (2-3%) coming from the knowledge of the acceptance. Discussion with the Hall A septum/optics expert [41], indicates that, in the worst case, the presence of the 5 T target field and the use of the septum will only increase the acceptance uncertainty by a factor of 2.

Eq. 17 reveals that the unmeasured low-x contribution to δ_{LT} is suppressed as x^2. In fact, over 90% of the total integral strength (as predicted from the MAID model) is covered in the range from pion threshold to $W = 1.7$ GeV for each of our incident energies. The unmeasured contribution above $W = 2$ GeV is very small and introduces a negligible uncertainty (See Fig. 16).

An 8%[‡] systematic uncertainty on δ_{LT}(Q^2) is shown as the gray band on the horizontal axis in Fig. 17.

4 Rates and Beam Time Request

The count rate of scattered electrons from the polarized target is given by:

$$\dot{N} = \frac{\mathcal{L}\Delta\Omega\Delta E'\sigma}{f} \tag{18}$$

where $\mathcal{L}$ is the luminosity, $\Delta\Omega$ is the angular acceptance, $\Delta E'$ is the momentum bite, σ represents the proton cross section, and f is the dilution factor which accounts for scattering from unpolarized nucleons in the target.

[†] as has been done in experiments E94010, E97110 and E01012.

[‡] relative to the MAID model prediction.

Source	(%)
Cross section	5-7
Target Polarization	3
Beam Polarization	3
Radiative Corrections	3
Parallel Contribution	< 1
^{15}N asymmetry [46]	< 1
Total	7-9

Table 2: Total Systematic Uncertainties.

Source	(%)
Acceptance	4-6
Packing fraction	3.0
Charge determination	1.0
VDC efficiency	1.0
PID detector efficiencies	$\leq$1.0
Software cut efficiency	$\leq$1.0
Energy	0.5
Deadtime	0.0
Total	5-7

Table 3: Breakdown of major contributions to the cross section systematic.

We estimate the experimental cross section by combining proton, nitrogen and helium cross sections from the quasifree scattering model QFS [36, 37]. Inelastic and elastic radiative effects are also included. Table 8 shows the assumed material thickness for a 3 cm target. At the lowest planned Q^2, the elastic radiative tail becomes large and we switch to a thinner (0.5 cm) target cell. Cross-checks with the longer standard cell will help to reduce the systematic uncertainty of the radiative corrections, and ensure we have a good understanding of our target packing fraction. A representative spin-independent cross section is shown in Fig. 18.

We estimate the time needed for a given uncertainty δA by:

$$T = \frac{1}{\dot{N}(fP_b P_T \delta A)^2} \tag{19}$$

The relevent statistical uncertainty is for the asymmetry, though this is a cross section measurement, because in the product σA the dominant error arises from A.

The running time and spectrometer configurations are summarized in Table 4. The sixth column represents the rate (in each bin) from the proton, while the seventh shows the total prescaled rate seen by the spectrometer.

When the momentum of the scattered electron is accessible by both spectrometers, we double our DAQ rate. We assume a maximum accessible momentum of 3.1 and 4.3 GeV for the right and left HRS respectively. We also assume both spectrometers can reach 0.4 GeV minimum momentum, and that the DAQ limit is 4 kHz per arm[§].

We will measure transverse data for every kinematic. Table 4 specifies the settings where we plan to also take data with the target polarization held parallel to the beam momentum. This is in order to directly extract g_1 and provide a cross check with the EG4 data. This effectively doubles the time needed for this setting, so the kinematic to perform the longitudinal measurement has been chosen to be at the largest Q^2 for which both arms can simultaneously take data for all chosen momentum settings.

To reach the highest Q^2 will require the septum to run 391 A at 6 degrees (P_0=4.15 GeV) and almost 530 A at 9 degrees (P_0=4.0 GeV). Discussion with Hall A septum experts [41, 42] indicate that all of the planned 6 degree settings should be achievable, although the septum must be trained to reach a few of the higher currents required. All of the 9 degree settings are also within the nominal limits, but the 9 degree, 4.0 GeV setting in particular may prove difficult. This has minimal impact on the physics goals of this experiment, since it affects only one kinematic setting at the highest Q^2 (see Fig. 5), whereas our main focus is at low Q^2. To adjust to this circumstance we can perform an extrapolation for the small affected region, or simply reduce our highest expected Q^2 by a small amount.

The choice of parameters used in our rate calculation is summarized in Table 8. We assume an angular acceptance of 4 msr and a momentum acceptance of $\pm 4\%$, both slightly reduced from the nominal values due to the presence of the septa, and beam and target polarizations of 80 and 75% respectively. We note that higher polarization

[§]More than 5 kHz rate with manageable deadtime was demonstrated with the existing DAQ during E97110 [10].

values are routinely achieved. Finally, we assume that the minimum time that we would reasonably spend at each setting is one half hour, regardless of how high the rate is.

With this beam request, we achieve $\delta A_\perp = 0.004$ for each 20 MeV bin.

4.1 Overhead

The incident beam causes radiation damage in the frozen ammonia, which leads to the creation [38, 39] of atomic hydrogen in the target material. This provides an additional relaxation path for the nuclear spins, and the buildup of these 'free radicals' leads to a gradual decay of the target polarization. The concentration of these unwanted radicals can be reduced significantly by raising the temperature of the target to 80-90K, in a process known as annealing. Given the proposed beam current and raster size, we expect to require an anneal about once every 14 hours of beam time. The anneal itself typically requires 2.5 hours from start to beam back on target. The target stick holds two ammonia batches. Each batch can absorb approximately $17{\cdot}10^{15}$ e-/cm^2, at which point the target must be replaced. We expect to replace the target material about once every 5 days of accumulated (100% efficient) beam. To replace the stick and calibrate the NMR instrumentation requires about a shift.

Measuring g_1 will require physically rotating the target can from the perpendicular to parallel configuration, a process which we estimate will take two shifts. One final overhead arising from the target comes from the need for dedicated empty cell and carbon target runs, which are used to determine the granular target packing fraction and dilution factor. These high rate unpolarized runs can be completed in about one half hour, and we plan to perform them for every other momentum setting.

Pass changes and linac changes are estimated to require 4 and 8 hours respectively. Changing the spectrometer momentum settings requires approximately 15 minutes each on average, while changes to the septa angle typically takes one shift. We will perform one Moller measurement for each beam energy, each of which requires two hours. Finally, we have included an additional 8 hours of overhead to measure the elastic cross section and asymmetry for the lowest two energies, as a cross check of our beam and target polarizations, and to help ensure we fully understand all cross section systematics.

The overhead requirement is summarized in Table 6. We note that previous experience has shown that many overhead tasks can be performed in parallel, or scheduled to coincide with non-delivery of beam. In this sense, our overhead estimate should be quite conservative.

4.2 Projected Results

Fig. 17 shows the projected accuracy we can obtain with the beam time request of Table 4. The systematic error band on the axis represents the total from Table 2. The projected uncertainties have been evaluated assuming the central value predicted by the MAID model [21].

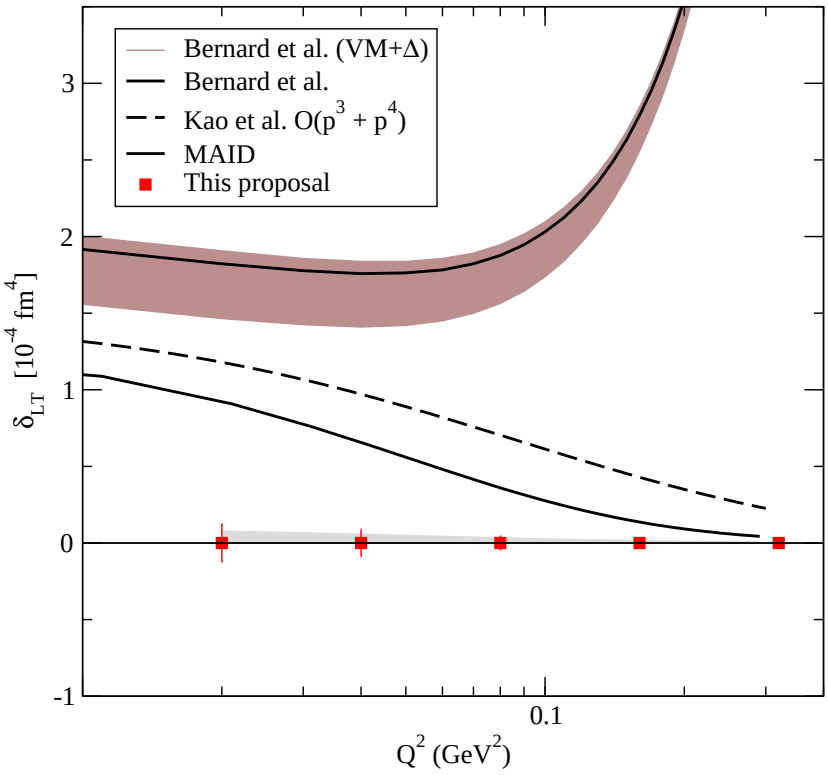

Figure 17: Projected results for δ_{LT}. Statistical errors are shown on the symbols. Systematic is represented by the grey band on the axis. Uncertainties are evaluated assuming the central value predicted by the MAID [21] model. χPT predictions from Bernard *et al.* [14], and Kao *et al.* [15].

5 Summary

State-of-art next-to-leading-order Chiral Perturbation calculations exhibit reasonable agreement with the proton and neutron's first moment Γ_1, and also with the neutron spin polarizability γ_0^n at the lowest Q^2 where they have been measured. However, there is a large discrepancy for δ_{LT}^n at Q^2 of 0.1 GeV^2. This is unexpected since δ_{LT} should be a good quantity to test χPT due to its insensitivity to the Δ resonance contribution.

We request 24 days in order to perform a measurement of $\delta_{LT}^p(Q^2)$ with 8% systematic uncertainty in the Q^2 range where χPT is expected to work well. The statistical accuracy will be comparable to the systematic and will allow an unambiguous test of the χPT calculations. Using a transversely polarized proton (NH_3) target, together with the Hall A HRS and septum, a precision measurement of g_2^p can be performed. Combined with the existing CLAS g_1^p data, δ_{LT}^p can be extracted to high precision. This data will help shed light on the δ_{LT} puzzle by providing the isospin dependence of the δ_{LT} polarizabilities. This data will also help to reduce the systematic uncertainty of γ_0^p measurements which arises from the model dependence of the transverse input. The Q^2-evolution of the proton $d_2(Q^2)$, BC Sum, and GDH Sum will also be obtained.

A Beam Request Tables

In this section we detail the proposed kinematics and beam time request. In Table 4, all energies and momenta are in GeV, while the luminosity is given in $(\text{cm}^2\text{-s})^{-1}$.

Table 6 summarizes the expected overhead, which was discussed in section 4.1. The expected statistical error is given in Table 7. Table 4 specifies whether we will measure data in the perpendicular configuration alone, or in both perpendicular and parallel configuration for each kinematic. Finally, for reference, in Table 8 we list the relevent experimental parameters that we have assumed in the rate calculation.

Table 4: Beam Time Request.

E_0	Θ	P_0	W	Q^2	Rate P (Hz)	Rate (kHz)	Pre	$\mathcal{L}$	$P_b P_t$	I (nA)	Time (h)
1.1	6	0.950	1.07	0.011	55	4.0	6	0.1E+35	0.60	85	6.7
1.1	6	0.871	1.14	0.010	58	4.0	4	0.1E+35	0.60	85	6.5
1.1	6	0.800	1.20	0.010	70	4.0	3	0.1E+35	0.60	85	5.3
1.1	6	0.734	1.25	0.009	82	4.0	3	0.1E+35	0.60	85	4.5
1.1	6	0.674	1.29	0.008	86	4.0	2	0.1E+35	0.60	85	4.3
1.1	6	0.618	1.33	0.007	93	4.0	2	0.1E+35	0.60	85	4.0
1.1	6	0.567	1.37	0.007	103	4.0	2	0.1E+35	0.60	85	3.6
1.1	6	0.521	1.40	0.006	113	4.0	2	0.1E+35	0.60	85	3.3
1.1	6	0.478	1.43	0.006	125	4.0	2	0.1E+35	0.60	85	3.0
1.1	6	0.439	1.45	0.005	139	4.0	2	0.1E+35	0.60	85	2.7
1.1	6	0.403	1.48	0.005	154	4.0	2	0.1E+35	0.60	85	2.4
1.1	6	0.369	1.50	0.004	170	4.0	2	0.1E+35	0.60	85	2.2
										1.0	days
1.7	6	1.540	1.07	0.029	46	4.0	2	0.1E+35	0.60	85	8.0
1.7	6	1.414	1.18	0.026	54	4.0	2	0.1E+35	0.60	85	6.9
1.7	6	1.297	1.27	0.024	66	4.0	1	0.1E+35	0.60	85	5.6
1.7	6	1.191	1.35	0.022	65	4.0	1	0.1E+35	0.60	85	5.7
1.7	6	1.093	1.41	0.020	72	4.0	1	0.1E+35	0.60	85	5.1
1.7	6	1.003	1.47	0.019	83	4.0	1	0.1E+35	0.60	85	4.5
1.7	6	0.920	1.53	0.017	93	4.0	1	0.1E+35	0.60	85	4.0
1.7	6	0.845	1.57	0.016	96	4.0	1	0.1E+35	0.60	85	3.9
1.7	6	0.775	1.61	0.014	98	3.9	1	0.1E+35	0.60	85	3.8
1.7	6	0.712	1.65	0.013	103	3.8	1	0.1E+35	0.60	85	3.6
1.7	6	0.653	1.68	0.012	113	4.0	1	0.1E+35	0.60	85	3.3
1.7	6	0.599	1.71	0.011	122	4.0	1	0.1E+35	0.60	85	3.1
1.7	6	0.550	1.74	0.010	129	4.0	1	0.1E+35	0.60	85	2.9
1.7	6	0.505	1.76	0.009	138	4.0	1	0.1E+35	0.60	85	2.7
1.7	6	0.463	1.79	0.009	147	4.0	1	0.1E+35	0.60	85	2.5

continued on next page

Table 4: Beam Time Request.

E_0	Θ	P_0	W	Q^2	Rate P (Hz)	Rate (kHz)	Pre	$\mathcal{L}$	$P_b P_t$	I (nA)	Time (h)
1.7	6	0.425	1.81	0.008	158	4.0	1	0.1E+35	0.60	85	2.4
1.7	6	0.390	1.83	0.007	170	4.0	1	0.1E+35	0.60	85	2.2
										1.5	days
2.2	6	2.030	1.07	0.049	45	4.0	13	0.8E+35	0.60	85	8.2
2.2	6	1.863	1.21	0.045	54	4.0	11	0.8E+35	0.60	85	6.9
2.2	6	1.709	1.33	0.041	58	4.0	8	0.8E+35	0.60	85	6.4
2.2	6	1.569	1.42	0.038	65	4.0	6	0.8E+35	0.60	85	5.7
2.2	6	1.440	1.51	0.035	77	4.0	5	0.8E+35	0.60	85	4.9
2.2	6	1.321	1.58	0.032	80	4.0	5	0.8E+35	0.60	85	4.7
2.2	6	1.213	1.64	0.029	83	4.0	4	0.8E+35	0.60	85	4.5
2.2	6	1.113	1.70	0.027	87	4.0	4	0.8E+35	0.60	85	4.3
2.2	6	1.022	1.75	0.025	89	4.0	4	0.8E+35	0.60	85	4.2
2.2	6	0.938	1.80	0.023	93	4.0	4	0.8E+35	0.60	85	4.0
2.2	6	0.860	1.84	0.021	96	4.0	5	0.8E+35	0.60	85	3.9
2.2	6	0.790	1.87	0.019	101	4.0	5	0.8E+35	0.60	85	3.7
2.2	6	0.725	1.91	0.017	107	4.0	5	0.8E+35	0.60	85	3.5
2.2	6	0.665	1.94	0.016	113	4.0	5	0.8E+35	0.60	85	3.3
2.2	6	0.610	1.96	0.015	120	4.0	6	0.8E+35	0.60	85	3.1
2.2	6	0.560	1.99	0.013	128	4.0	6	0.8E+35	0.60	85	2.9
2.2	6	0.514	2.01	0.012	137	4.0	7	0.8E+35	0.60	85	2.7
										1.6	days
3.3‡	6	3.096	1.07	0.112	29	4.0	7	0.8E+35	0.60	85	12.7
3.3‡	6	2.841	1.28	0.103	39	4.0	6	0.8E+35	0.60	85	9.4
3.3‡	6	2.608	1.44	0.094	42	4.0	4	0.8E+35	0.60	85	8.7
3.3‡	6	2.393	1.58	0.087	50	4.0	3	0.8E+35	0.60	85	7.5
3.3‡	6	2.196	1.69	0.079	54	4.0	2	0.8E+35	0.60	85	6.9
3.3‡	6	2.016	1.79	0.073	57	4.0	2	0.8E+35	0.60	85	6.5
3.3‡	6	1.850	1.88	0.067	61	4.0	2	0.8E+35	0.60	85	6.1
3.3‡	6	1.698	1.96	0.061	65	4.0	1	0.8E+35	0.60	85	5.7
3.3‡	6	1.558	2.02	0.056	69	4.0	1	0.8E+35	0.60	85	5.4
										2.9	days
4.4	6	4.149†	1.07	0.200	22	4.0	5	0.8E+35	0.60	85	16.7
4.4	6	3.808†	1.34	0.184	29	4.0	4	0.8E+35	0.60	85	12.9
4.4	6	3.495†	1.55	0.168	33	4.0	2	0.8E+35	0.60	85	11.4
4.4	6	3.207†	1.72	0.155	34	4.0	2	0.8E+35	0.60	85	10.7
4.4	6	2.944	1.86	0.142	36	4.0	1	0.8E+35	0.60	85	10.3

continued on next page

Table 4: Beam Time Request.

E_0	Θ	P_0	W	Q^2	Rate P (Hz)	Rate (kHz)	Pre	$\mathcal{L}$	$P_b P_t$	I (nA)	Time (h)
4.4	6	2.701	1.98	0.130	40	4.0	1	0.8E+35	0.60	85	9.4
4.4	6	2.479	2.09	0.120	44	4.0	1	0.8E+35	0.60	85	8.4
										2.7	days
4.4	9	4.023†	1.07	0.436	14	2.5	1	0.8E+35	0.60	85	25.2
4.4	9	3.692†	1.34	0.400	17	2.2	1	0.8E+35	0.60	85	21.4
4.4	9	3.389†	1.55	0.367	16	2.0	1	0.8E+35	0.60	85	22.4
4.4	9	3.110†	1.72	0.337	14	1.7	1	0.8E+35	0.60	85	25.6
4.4	9	2.854	1.86	0.309	12	1.4	1	0.8E+35	0.60	85	31.2
4.4	9	2.620	1.98	0.284	11	1.2	1	0.8E+35	0.60	85	33.1
4.4	9	2.404	2.09	0.260	11	1.1	1	0.8E+35	0.60	85	33.7
										6.0	days

† signifies that only the left spectrometer can access this momentum.
‡ signifies that longitudinal data will be taken in addition to transverse.

Table 5: Beam Request Summary.

Days using 1 (2) arms	25.2(15.7)
Days for Overhead	8.4(8.4)
Total Days using 1 (2) arms	33.6(24.1)

Table 6: Overhead

Overhead	Number	Time Per (hr)	(hr)
Target anneal	27	2.5	67.5
Target rotation	2	16.0	32.0
Target swap	2	8.0	16.0
Pass change	6	4.0	24.0
Packing Fraction	34	0.50	17.0
Linac change	0	8.0	0.0
Momentum change	69	0.25	17.2
Moller measurement	6	2.0	12.0
Septum angle change	1	8.0	8.0
Elastic calibration	2	4.0	8.0
			201.8

Table 7: Statistical Uncertainty

Kinematic	$A_{\parallel}$ error	$A_{\perp}$ error
1	0.004*	0.004
2	0.004*	0.004
3	0.004*	0.004
4	0.004	0.004
5	0.004*	0.004
6	0.004*	0.004

* EG4 expected uncertainty.

Table 8: Experiment Parameters

Parameter	Value
$\Delta\Omega$ [msr]	4.0
$\pm\delta P$[%]	4.0
P_{Target} [%]	75.0
P_{Beam} [%]	80.0
T_b	0.026
T_a	0.026
Minimum time per setting [hr]	0.5
Minimum Momentum [MeV]	400.0
Maximum Momentum (L) [MeV]	4300.0
Maximum Momentum (R) [MeV]	3100.0
Daq Limit [kHz]	4.0
Packing Fraction	0.55

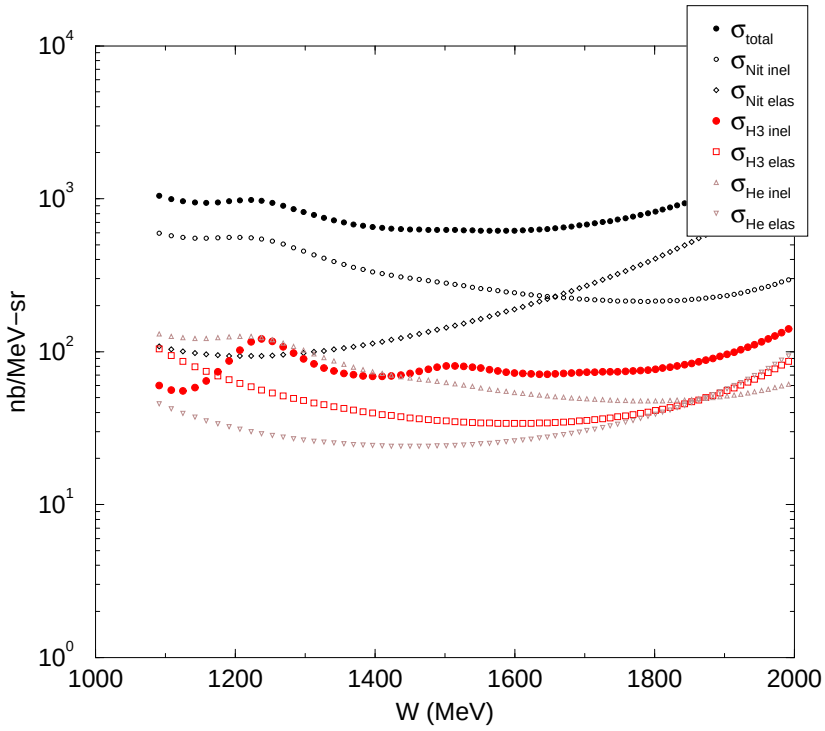

Figure 18: NH_3 cross section at $E_0 = 2.2$ GeV, 6°.

References

[1] See, *e.g.*, B. W. Filippone and X. Ji, Adv. Nucl. Phys. **26**, 1 (2001).

[2] J. D. Bjorken, Phys. Rev. **148**, 1467 (1966).

[3] M. Amarian *et al.*, Phys. Rev. Lett. **89**, 242301 (2002);**92**, 022301 (2004);**93**, 152301 (2004); K. Slifer, *et al.*, to be submitted to Phys. Rev. Lett.

[4] R. Fatemi *et al.*, Phys. Rev. Lett. **91**, 222002 (2003).

[5] J. Yun *et al.*, Phys. Rev. **C 67**, 055204 (2003).

[6] A. Deur *et al.*, Phys. Rev. Lett. **93**, 212001 (2004).

[7] K.V. Dharmawardane *et al.*, Phys. Lett. **B 641** 11 (2006); Y. Prok *et al.*, to be published.

[8] JLab RSS experiment, M. Jones and O Rondon, spokespersons. nucl-ex/0608003

[9] J.-P. Chen, A. Deur and Z.-E. Meziani, Mod. Phys. Lett. **A 20**, 2745 (2005); J.-P. Chen, nucl-ex/0611024 (2006).

[10] JLab experiment E97-110, J. P. Chen, A. Deur, F. Garibaldi, spokespersons.

[11] JLab run group eg4, M. Battaglieri, R. De Vita, A. Deur, M. Ripani spokespersons.

[12] JLab E01-012, J. P. Chen, S. Choi and N. Liyanage, spokespersons.

[13] K. Abe *et al.*, Phys. Rev. **D 58**,112003 (1998); P. L. Anthony, *et al.*, Phys. Lett. **B 493**, 19 (2000), **B 553**, 18 (2003).

[14] V. Bernard, T. Hemmert and Ulf-G. Meissner, Phys. Lett.

[15] C. W. Kao, T. Spitzenberg and M. Vanderhaeghen, Phys. Rev. **D 67**, 016001 (2003).

[16] Kochelev, PRD67, 074014 (2003) and private communication.

[17] N. I. Kochelev et al, Phys. Rev. D **67**, 074014 (2003).

[18] Marc Vanderhagen, private communication.

[19] C. Weiss private communication.

[20] S. B. Gerasimov, Sov. J. Nucl. Phys. **2**, 598 (1965); S. D. Drell and A. C. Hearn, Phys. Rev. Lett. **16**, 908 (1966).

[21] D. Drechsel, S. S. Kamalov and L. Tiator, Phys. Rev. **D 63**, 114010 (2001).

[22] X. Ji and J. Osborne, J. of Phys. G **27**, 127 (2001).

[23] D. Drechsel, B. Pasquini and M. Vanderhaeghen, Phys. Rep. **378**, 99 (2003); D. Drechsel and L. Tiator, Ann. Rev. Nucl. Part. Sci. **54**, 69 (2004).

[24] H. Burkhardt and W. N. Cottingham, Ann. Phys. (N.Y.) **56**, 453 (1970).

[25] S. Wandzura and F. Wilczek, Phys. Lett. **B72**, 195 (1977).

[26] K. Ackerstaff *et al.*, Phys. Lett. **B 404**, 383 (1997); **B 444**, 531 (1998).

[27] X. Ji, C. Kao, and J. Osborne, Phys. Lett. B **472**, 1 (2000). **B 545**, 105 (2002); Phys. Rev. **D 67**, 076008 (2003).

[28] J. Soffer and O. V. Teryaev, Phys. Rev. **D 70**, 116004 (2004).

[29] V. D. Burkert and B. L. Ioffe, Phys. Lett. **B 296**, 223 (1992).

[30] Y. Prok *et al.* In preparation. See for example A. Deur, presentation at the APS-DNP06 meeting (2006).

[31] JLab experiment E06-014, S. Choi, X. Jiang, Z.E. Meziani and B. Sawatzky spokespersons.

[32] JLab experiment E12-06-121, T. Averett, W. Korsch, Z.E. Meziani and B. Sawatzky, spokespersons.

[33] M. Gockeler *et al.*, Phys. Rev. **D 63**, 074506, (2001).

[34] X. Zheng *et al.*, Phys. Rev. **C 70**, 065207 (2004).

[35] K. Slifer [RSS collaboration], in preparation.

[36] J.W. Lightbody Jr. and J.S. O'Connell, Computers in Physics,57 May/June 1988.

[37] K. Slifer, E94010 Collaboration technote TN-E94010-44.

[38] P. M. McKee NIM A526 (2004) 60-64.

[39] L. De Marco, A, Brill, D. Crabb, J. Chem. Phys. 108 (1998) 1423.

[40] M. Amarian *et al.* [Jefferson Lab E94-010 Collaboration], Phys. Rev. Lett. **92**, 022301 (2004) [arXiv:hep-ex/0310003].

[41] J. Lerose, Hall A Staff. Private communication.

[42] R. Feuerbach, Hall A Staff. Private communication.

[43] K. Slifer, E94010 Technical Note #37 : "Dependence of the Cross-Section on Acceptance Cuts for E94010", (2001)

[44] K. Slifer, E94010 Technical Note #38 : "E94010 Unpolarized ^{3}He Cross Sections", (2001)

[45] K. Slifer, Ph.D. Thesis. Temple University (2004).

[46] Mark Jones, "*The ^{15}N correction to the measured asymmetries*", RSS technical note 2005-01 (2005).

[47] M. Ripani's EG4 analysis webpage : http://www.jlab.org/Hall-B/secure/eg4/ripani/analysis.html

[48] JLab E05-004 : R. Gilman, D.W. Higinbotham, X. Jiang, spokespersons. '$A(Q)$ at low Q in ed Elastic Scattering'.

[49] Private communication, Arne Freyberger.

[50] L. Kaufman, K. Pascke, R. Michaels, "Cavity Monitor Performance in 2005", http://hallaweb.jlab.org/experiment/HAPPEX/docs/, HAPPEX technote, (2006).

[51] C. Yan, R. Carlini, "Chicane and raster system for Hall C", CEBAF-R-92-004, (1992).

[52] J. Alcorn *et al.*, Nucl. Instrum. Meth. A **522**, 294 (2004).

[53] J. W. Lightbody, Jr., J. S. O'Connell, Computers in Physics, May/June (1988).